Macromolecules

ARTICLE

pubs.acs.org/Macromolecules

Confinement-Induced High-Field Antiferroelectric-like Behavior in a Poly(vinylidene fluoride-*co*-trifluoroethylene-*co*-chlorotrifluoroethylene)-*graft*-polystyrene Graft Copolymer

Fangxiao Guan,[†] Jing Wang,[†] Lianyun Yang,[§] Jung-Kai Tseng,[§] Kuo Han,[‡] Qing Wang,[‡] and Lei Zhu*[,†,§]

[†]Polymer Program, Institute of Materials Science and Department of Chemical, Materials and Biomolecular Engineering, University of Connecticut, Storrs, Connecticut 06269-3136, United States

[‡]Department of Materials Science and Engineering, Pennsylvania State University, University Park, Pennsylvania 16802, United States

[§]Department of Macromolecular Science and Engineering, Case Western Reserve University, Cleveland, Ohio 44106-7202, United States

Supporting Information

ABSTRACT: An antiferroelectric-like polymer approach was proposed for high electric energy storage and low loss performance by using a novel confinement concept. A poly(vinylidene fluoride-*co*-trifluoroethylene-*co*-chlorotrifluoroethylene)-*graft*-polystyrene [P(VDF-TrFE-CTFE)-*g*-PS] graft copolymer with 14 wt % PS side chains was successfully synthesized. On the basis of the electric displacement−electric field loop study, a novel antiferroelectric-like behavior with extremely low remanent polarization was achieved in this graft copolymer even when the poling field reached as high as 400 MV/m. Compared with a P(VDF-TrFE) random copolymer having the same TrFE content, a similar discharged energy density but a much lower hysteresis loss was observed. This novel antiferroelectric-like behavior at high poling fields was explained by the confinement (or insulation) effect. After crystallization-induced microphase separation, PS side chains were segregated to the periphery of P(VDF-TrFE) crystals, forming a nanoscale interfacial confining (or insulation) layer. Because of the low polarizability of this confining layer, the compensation polarization at the amorphous−crystalline interface was reduced, and thus the local polarization field became weaker than the local depolarization field. Upon discharging, therefore, a fast dipole reversal and an antiferroelectric-like behavior were achieved even at high poling fields. This study will help us design new polar dielectric polymers for high electric energy storage and low loss applications.

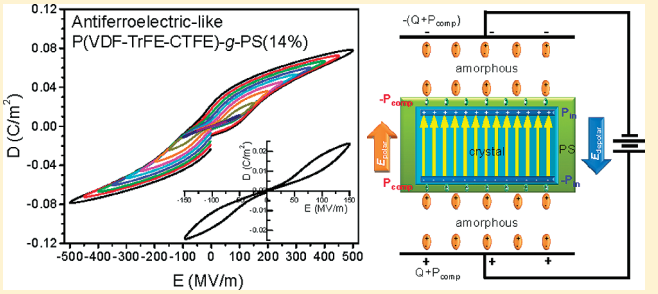

INTRODUCTION

Advanced pulsed power and power conditioning technologies for power generation/regulation and all electric vehicles/ships require a capacitor material to achieve a high discharged electric energy density (U_e) as well as low loss performance.[1−3] Since the energy density of a dielectric capacitor material is proportional to its permittivity and the square of the electric field, many efforts have been devoted to the enhancement of the material's permittivity and/or dielectric breakdown strength.[4−14] Recently, the combination of high permittivity nanoparticles and a high breakdown strength polymer matrix provides a potential to achieve high permittivity nanocomposite materials for high energy density capacitors.[7,8,15−18] Usually, the content of nanoparticles has to be above a certain threshold (i.e., the minimum percolation volume fraction of 30−35 vol % for spherical nanoparticles) to effectively increase the apparent permittivity.[19,20] For such a high volume fraction, the high permittivity nanoparticles tend to agglomerate and phase separate from the polymer matrix, resulting in poor processability, high defect density, and low breakdown strength because of the well-known effect of surface plasmon-enhanced local fields near agglomerated particles.[21]

Ferroelectric polymers based on poly(vinylidene fluoride) (PVDF) and its copolymers appear to be another choice because of their relatively high permittivity (10−20) and high dc breakdown strength (ca. 700 MV/m for a test area of 2 cm^2).[5,6,11,22,23] By modifying PVDF with bulky comonomers such as chlorotrifluoroethylene (CTFE) and hexafluoropropylene (HFP), P(VDF-CTFE) and P(VDF-HFP) random copolymers recently have achieved a discharged energy density as high as 17−25 J/cm^3 at ∼600 MV/m for millisecond discharge.[5,6] Nevertheless, ferroelectric polymers have relatively high losses due to the delayed dipole switching with respect to the alternating electric field. For example, the typical dielectric loss at low fields, tan δ, for PVDF and its copolymers is about 0.02,[24] substantially higher than that of the current state-of-the-art capacitor film, biaxially stretched polypropylene (BOPP, tan $\delta \sim 0.0002$).[25] At high electric fields, depending on the polymorphism (β- vs α-crystals), their ferroelectric

Received: September 9, 2010
Revised: January 20, 2011
Published: March 02, 2011

Scheme 1. Schematic Electric Displacement−Electric Field ($D-E$) Hysteresis Loops for (A) Normal Ferroelectrics, (B) Relaxor Ferroelectrics, and (C) Antiferroelectrics[a]

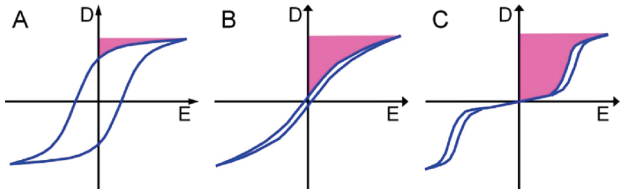

[a] The shaded areas represent the discharged energy density, and the loops represent the ferroelectric loss.

losses can be as high as 40−80% because of the ferroelectric hysteresis loops during switching (see Scheme 1A).[6,26,27] This ferroelectric loss is also discharge time dependent; an additional 40% loss in discharged energy density when the discharge time decreases from 1 ms to 1 μs.[6]

New strategies are actively pursued to reduce dielectric and ferroelectric losses in ferroelectric polymers, and the key is to understand fundamental dipole reorientation and switching mechanisms in response to an oscillating electric field. In our recent reports,[27,28] we have indicated that reducing the compensation polarization in ferroelectric polymers by confining ferroelectric domains can facilitate a fast dipole reorientation during discharge. In turn, the ferroelectric loss will be reduced and the discharged energy density will increase. One method for confining ferroelectric domains is to reduce the crystallite size (i.e., the upper limit for ferroelectric domains), and a relaxor-like ferroelectric behavior[29] with narrower hysteresis loops (see Scheme 1B) than those for normal ferroelectrics (see Scheme 1A) is obtained. This is exactly demonstrated in the above-mentioned P(VDF-CTFE) random copolymer with 9 mol % CTFE[5,6] and was further explained by computer simulation using the nanodomain concept.[30]

Here, we propose another novel approach—antiferroelectric-like polymers—to enhance the discharged energy density and to reduce the ferroelectric loss (see Scheme 1C). Antiferroelectric phases in ceramics[31−35] and liquid crystal[36] have attracted much attention because they have extremely low remanent polarization and relatively narrow electric displacement−electric field ($D-E$) hysteresis loops, indicating a relatively low ferroelectric loss.[32−36] Antiferroelectric-like behavior was also reported in PVDF and its random copolymers by showing propeller-shaped double hysteresis loops.[26,27,37−40] However, most antiferroelectric phases in ceramics/liquid crystals or antiferroelectric-like behavior in polymers only exist at relatively low electric fields (<100 MV/m for ceramics/liquid crystals and <200 MV/m for polymers). At high enough fields, antiferroelectric phases will transform into normal ferroelectric phases, and the antiferroelectric-like behavior eventually will be lost. Therefore, it is still challenging for conventional antiferroelectric materials to achieve high discharged energy density at high electric fields.

In this work, we confined (or insulated) PVDF lamellar crystals with a low polarizability polystyrene (PS) interfacial layer to reduce the compensation polarization in PVDF copolymers during bipolar poling processes. The antiferroelectric-like behavior was observed even at a poling electric field as high as 400 MV/m. Moreover, a significant reduction in the ferroelectric loss was achieved with only a slight decrease in the discharged energy density when compared to the PVDF copolymer without confinement.

EXPERIMENTAL SECTION

Materials. P(VDF-CTFE) samples (Dyneon 31008 and 31508 with 7.0 and 11.2 mol % CTFE) were provided by courtesy of 3M. Their number-average molecular weights (M_n) were ca. 70 400 and 93 400 g/mol, and the polydispersity indices (PDI) were 2.3 and 2.1 for Dyneon 31008 and 31508, respectively. Statistically, each main chain contained ca. 73 and 150 Cl sites in Dyneon 31008 and 31508, respectively. P(VDF-HFP) 96/4 pellets were purchased from Aldrich, which contained 4 mol % HFP comonomer as determined by fluorine nuclear magnetic resonance (^{19}F NMR). Its number-average molecular weight is 130 000 g/mol, and the weight-average molecular weight is 400 000 g/mol. Styrene (Aldrich, 99%) was passed through a silica gel column to remove the inhibitor before use. Azobis(isobutyronitrile) (AIBN) was recrystallized from methanol and stored in the refrigerator. Cu(I)Cl (Aldrich, 99.995+%), Cu(II)Cl_2 (Aldrich, 99.999%), 2,2′-bipyridine (BPy, Acros, 99+%), tri(*n*-butyl)tin hydride (*n*Bu_3SnH, Aldrich, 99.99%), *N*-methylpyrrolidinone (NMP, Aldrich, HPLC grade), tetrahydrofuran (THF, Aldrich, HPLC grade), and *N*,*N*-dimethylformamide (DMF, Acros, HPLC grade) were used as received without further purification.

Dechlorination of P(VDF-CTFE). The dechlorination of the P(VDF-CTFE) was adapted from a previous report,[10] and here we use P(VDF-CTFE) 88.8/11.2 as an example. First, a 500 mL round-bottom flask was charged with 4.0 g of P(VDF-CTFE) copolymer, 1.371 g (8 mmol) of AIBN, 100 mL of THF, and 100 mL of NMP. The reaction solution was purged with nitrogen for about 1 h. Afterward, the reaction mixture was stirred at 60 °C for 30 min, and 4.397 mL (16.02 mmol) of *n*Bu_3SnH was added dropwise using a syringe. The dechlorination reaction was carried out at 60 °C for 24 h before it was quenched with methanol. The reaction mixture was precipitated in a 1:1 vol/vol methanol/water mixture and washed with *n*-hexane. The crude product was redissolved in DMF and precipitated in 1:1 methanol/water for three times. Finally, the product was dried in a vacuum oven at room temperature for 3 days before its usage as a macroinitiator for the graft copolymerization of styrene. Note that P(VDF-CTFE) 88.8/11.2 was only partially dechloronated, and a terpolymer, P(VDF-TrFE-CTFE) 88.8/7.7/3.5, where TrFE represented trifluoroethylene, was obtained. P(VDF-CTFE) 93/7 was fully dechloronated, and a copolymer P(VDF-TrFE) 93/7 was obtained.

Graft Copolymerization of Styrene from P(VDF-TrFE-CTFE) Terpolymer Using ATRP. The graft copolymerization of styrene from P(VDF-TrFE-CTFE) using atom transfer radical polymerization (ATRP) was modified from a previous report (Scheme 2).[41] First, a 500 mL Schlenk flask was charged with 2.0 g of P(VDF-TrFE-CTFE), 2.33 g (14.89 mmol) of 2,2′-bipyridine, 0.4 g (4.02 mmol) of CuCl, and 54.3 mg (0.402 mmol) of $CuCl_2$. The reaction mixture was degassed for three times with dry nitrogen−vacuum cycles. 23 mL (205 mmol) of styrene and 28 mL of NMP were purged with dry nitrogen for about 1 h and transferred into the Schlenk flask by a nitrogen-protected syringe. After all reaction agents were well mixed, the polymerization was carried out at 120 °C for 24 h. The viscous reaction mixture was diluted with acetone and passed through a column filled with fumed silica gel, followed by precipitation in a 1:1 methanol/water mixture. The crude product was redissolved in DMF and precipitated in a 1:1 methanol/water mixture for three times. Finally, the resulting graft copolymer, P(VDF-TrFE-CTFE)-*g*-PS(14%), was dried in a vacuum oven at room temperature for 2 days. Finally, the dechlorination reaction of the as-synthesized P(VDF-TrFE-CTFE)-*g*-PS(14%) was carried out in a similar method as that for the dechlorination reaction of P(VDF-CTFE) described above.

Film Fabrication and Processing. Thick films with a thickness around 80−100 μm were prepared by hot-pressing the P(VDF-TrFE-CTFE)-*g*-PS(14%) graft copolymers at 240 °C followed by immediate quenching into ice/water. Then, the hot-pressed thick films were

Scheme 2. Synthesis of P(VDF-TrFE-CTFE)-*g*-PS Graft Copolymer Using ATRP, Followed by Dechlorination with nBu$_3$SnH To Avoid Thermal Cross-Linking during Later Melt Processing

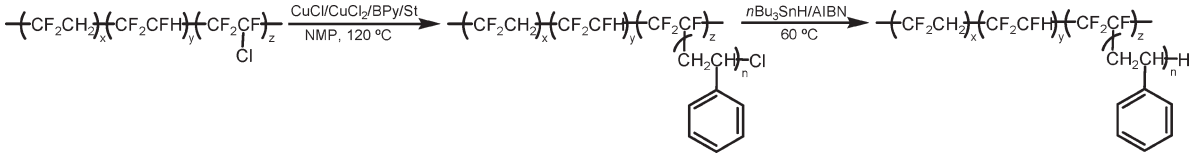

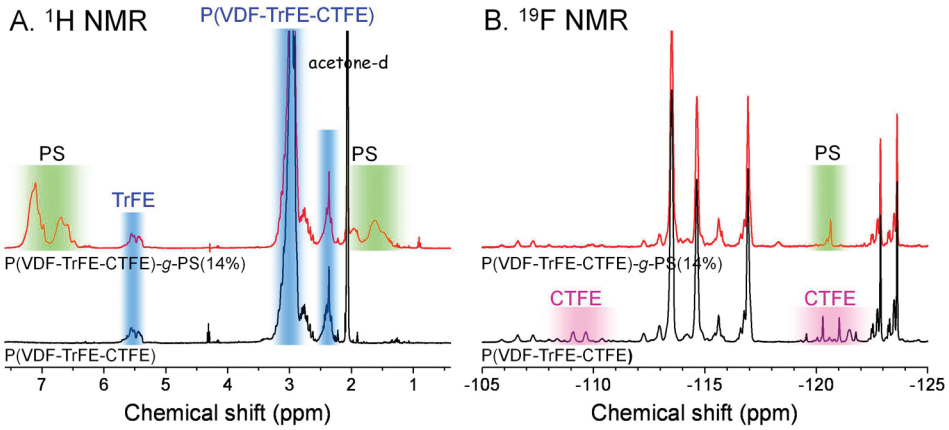

Figure 1. (A) ^{1}H and (B) ^{19}F NMR spectra of P(VDF-CTFE-TrFE) 88.8/7.7/3.5 and P(VDF-CTFE-TrFE)-*g*-PS(14%), respectively. In the ^{1}H NMR spectra in (A), PS and P(VDF-CTFE-TrFE) peaks are highlighted with green and blue colors. In the ^{19}F NMR spectra in (B), Cl-related F atoms are highlighted with magenta color and F atoms related to PS side chains are highlighted with green color.

uniaxially stretched at 110 °C to a ~600% extension ratio at 12.7 mm/min. The solution-cast P(VDF-HFP) 96/4 film (ca. 50 μm thick) was prepared by slow solution-casting from 4 wt % solution of P(VDF-HFP) 96/4 in THF at room temperature, and it was then uniaxially stretched (~650% extension ratio) at 60 °C to achieve a final thickness around 8 μm.[27] For detailed structural characterization results of this film, refer to ref 27.

Instrumentation and Characterization. ^{1}H and ^{19}F NMR spectra were recorded on a Bruker spectrometer (500 MHz, DMX 500). Differential scanning calorimetry (DSC) thermograms were obtained using a TA Instruments Q20 DSC at a scanning rate of 10 °C/min. Fourier transform infrared (FTIR) was performed on a Nicolet Nexus 870 FTIR spectrometer. Two-dimensional (2D) small-angle X-ray scattering (SAXS) was performed on a Rigaku SAXS instrument with an 18 kW rotating anode X-ray generator (MacroMax 002+) operating at 45 kV and 0.88 mA. 2D wide-angle X-ray diffraction (WAXD) experiments were performed on an Oxford Xcalibur diffractometer with an ONYX CCD area detector. The X-ray wavelength (λ) was Cu Kα 0.1542 nm. One-dimensional (1D) WAXD profiles were obtained by integrating the corresponding 2D WAXD images. The *d*-spacing was calibrated using silver behenate with the first-order reflection at a scattering vector $q = 1.076$ nm^{-1}, where $q = (4\pi \sin\theta)/\lambda$ with θ being the half scattering angle.

The real and imaginary relative permittivity, ε_r' and ε_r'', in a frequency range from 20 to 10^6 Hz were measured using an Agilent 4284A Precision LCR meter at a bias voltage of 1 V. Polarization hysteresis loops at room temperature were collected using a modified Sawyer–Tower circuit at 10 Hz.[6] Gold electrodes were sputtered onto both surfaces of the film with a thickness around 50 nm. The gold electrode area was ca. 0.0531 cm^2 for the $D-E$ loop measurements. Stored and released energy densities (U_e) were obtained by integrating the corresponding charging and discharging curves, $U_e = \int E\, dD$. Details should refer to the experimental setup for energy density measurements in the Supporting Information.

RESULTS AND DISCUSSION

Synthesis of P(VDF-TrFE-CTFE)-*g*-PS Graft Copolymer. On the basis of a previous study,[27] we purposely choose P(VDF-TrFE) as the main chain polymer for grafting polymerization mainly because of two reasons. First, a certain amount of TrFE commoners in the PVDF main chain can facilitate the formation of β-crystals.[23] Second, a high β crystal content with small crystallite sizes is necessary for high discharged energy density with a relatively low loss.[27] The precursor polymer, P(VDF-TrFE-CTFE) terpolymer, was synthesized by partial dechlorination of a P(VDF-CTFE) with 11.2 mol % CTFE.[10] Calculation from ^{1}H NMR in Figure 1A showed that this terpolymer had 7.7 mol % TrFE, 3.5 mol % CTFE, and 88.8 mol % VDF. The CTFE units were used as the initiation sites for the grafting polymerization of styrene by using ATRP (see Scheme 2).[41] Although it was desired to utilize a P(VDF-TrFE-CTFE) terpolymer with a higher TrFE content (e.g., >30 mol %) for the preferred β-crystals, we were limited by the commercially available P(VDF-CTFE) copolymer with a maximum CTFE content of 11.2 mol %. In the future, we will continue to study P(VDF-TrFE-CTFE)-*g*-PS graft copolymers with higher TrFE contents.

Successful grafting of PS side chains from the Cl sites in P(VDF-TrFE-CTFE) was proved by ^{19}F NMR, as shown in Figure 1B. Comparing the ^{19}F NMR spectra for P(VDF-TrFE-CTFE) and its PS-graft copolymer, the Cl-related F signals disappeared at chemical shift ranges from −108 to −112 ppm and −119 to −123 ppm, respectively, and a new peak appeared at −121 ppm, which was assigned as the F atoms related to the PS side chains. A control experiment by replacing P(VDF-TrFE-CTFE) with PVDF under the same ATRP reaction condition was also performed, and no PS could be grafted

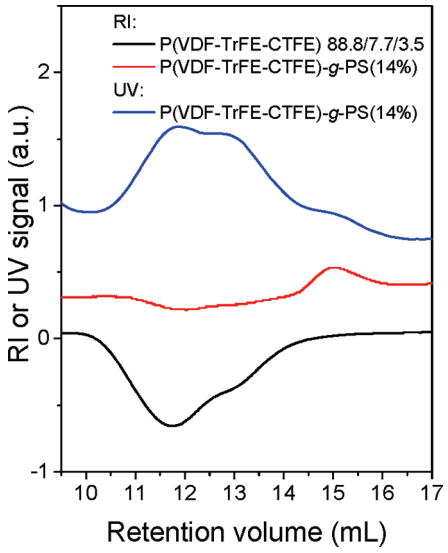

Figure 2. SEC curves for P(VDF-TrFE-CTFE) 88.8/7.7/3.5 (RI signal) and P(VDF-TrFE-CTFE)-*g*-PS(14%) (RI and UV signals). DMF is used as the solvent at a flow rate of 1.0 mL/min.

from the neat PVDF. This result indicated that PS side chains were exclusively grafted from the Cl sites in P(VDF-TrFE-CTFE). Calculation from ^{1}H NMR in Figure 1A showed that 14 wt % PS (average 3.2 styrene repeating units per PS side chain) was grafted onto the P(VDF-TrFE-CTFE) main chain. Therefore, the graft copolymer was denoted as P(VDF-TrFE-CTFE)-*g*-PS(14%).

Figure 2 shows SEC results for P(VDF-TrFE-CTFE)-*g*-PS-(14%) and its precursor terpolymer, P(VDF-TrFE-CTEF) 88.8/7.7/3.5. Because the refractive index (n) of P(VDF-TrFE-CTFE) 88.8/7.7/3.5 (n = 1.40−1.42) was lower than that of DMF (n = 1.43 at 25 °C), a broad negative peak was observed when using a differential refractive index (RI) detector. After grafting 14 wt % PS side chains, nearly no RI peak was observed because the overall refractive index of the graft copolymer matched that of DMF due to a higher refractive index for PS (n = 1.59). Therefore, we used a UV detector in SEC for the graft copolymer. However, the increase in hydrodynamic volume was not much because of its graft copolymer architecture. From the SEC results, no PS homopolymer was observed, and this was further confirmed by thin layer chromatography using toluene as the developing solvent on a silica gel plate.

Microphase and Crystalline Morphology Characterization. Before we proceed to study the crystalline morphology, it is desired to understand whether there is any microphase separation in the melt of the graft copolymers before crystallization. Figure 3 shows the SAXS profile for the P(VDF-TrFE-CTFE)-*g*-PS(14%) graft copolymers at 180 °C. Only a broad correlation-hole scattering could be observed with the center at $q^* = 0.25$ nm^{-1} (i.e., d-spacing of 25.1 nm), suggesting that the PS side chains did not microphase separate from the P(VDF-TrFE) main chain but forming a density fluctuation-induced disordered phase in the melt.[42,43] We speculate that too short PS chain, too many grafting sites on the main chain, and broad molecular weight distributions resulted in the disordered phases in the graft copolymers.

Thick films (~100 μm) of the P(VDF-TrFE-CTFE)-*g*-PS-(14%) graft copolymer was prepared by hot-pressing the sample at 240 °C followed by quickly quenching into ice water. The

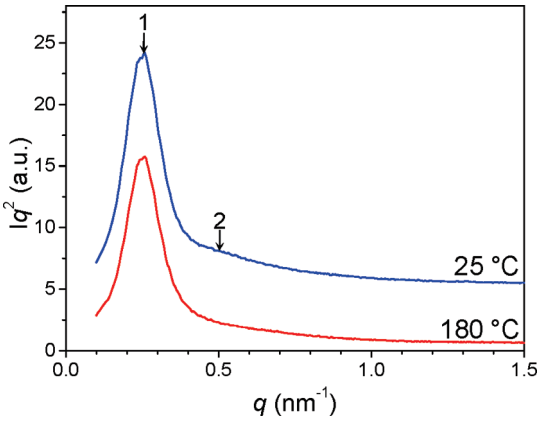

Figure 3. Lorentz-corrected SAXS profile for the P(VDF-TrFE-CTFE)-*g*-PS(14%) graft copolymer at 180 °C and cooling naturally back to 25 °C.

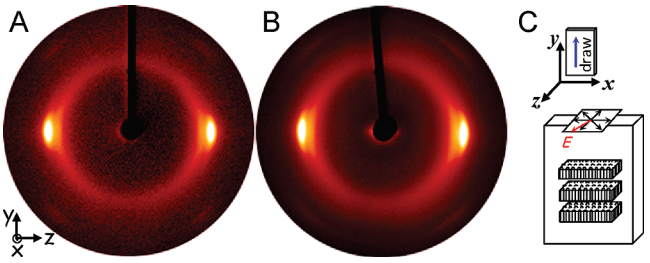

Figure 4. 2D WAXD patterns for (A) P(VDF-TrFE) 93/7 and (B) P(VDF-TrFE-CTFE)-*g*-PS(14%) when the X-ray beam was directed along the x direction. (C) shows the mechanical drawing direction and the crystal orientation in the films. Dipoles (black arrows) are oriented in a plane parallel to the external electric field (E) (the red arrow).

sample was then oriented by uniaxially stretching the thick film to an extension ratio of 500% at 110 °C to obtain a final film thickness of ~20 μm. Here, we chose a P(VDF-TrFE) 93/7 copolymer with 7 mol % TrFE as a control because the TrFE content was close to that in P(VDF-TrFE-CTFE)-*g*-PS(14%) (TrFE% = 7.7 mol %). The P(VDF-TrFE) film was processed using the same processing condition as that for P(VDF-TrFE-CTFE)-*g*-PS(14%).

The crystalline morphology in these films was characterized by two-dimensional (2D) wide-angle X-ray diffraction (WAXD). The crystals were oriented parallel to the drawing direction after mechanical stretching, as evidenced by the (hk0) reflections concentrated on the equator for films P(VDF-TrFE) 93/7 and P(VDF-TrFE-CTFE)-*g*-PS(14%), respectively (see Figure 4A,B). This crystal orientation is particularly preferred because all the dipoles, which are nearly perpendicular to the chain axes, can be readily responsive to the external electric field.[26] The actual α and β crystal contents and the crystallite sizes were calculated from the 1D WAXD profiles in Figure 5 (integrated along the z direction in the 2D WAXD patterns in Figure 4) and are summarized in Table 1. Details on the peak-fitting calculation can be found in our previous reports.[26,27] The overall crystallinity (32.6 wt %) in the P(VDF-TrFE-CTFE)-*g*-PS(14%) was lower than that (45.2 wt %) in P(VDF-TrFE) 93/7 because the 14 wt % PS was included in the amorphous part in the crystallinity calculation. Note that the dielectric and ferroelectric properties of these films are primarily determined by the overall crystallinity rather than the crystallinity only with respect to PVDF. The β crystal content (6.5%) in

P(VDF-TrFE-CTFE)-*g*-PS(14%) was lower than that (17.6%) in P(VDF-TrFE) 93/7 because the phase transformation from α- to *β*-crystals was hindered by attaching large PS side chains to the P(VDF-TrFE-CTFE) main chain. The estimated crystallite sizes (14−19 nm) in P(VDF-TrFE-CTFE)-*g*-PS(14%) was similar to that (17 nm) in P(VDF-TrFE) 93/7.

Dielectric and Antiferroelectric-like Properties. The effect of grafting PS side chains on the dielectric response at low electric fields (bias voltage = 1 V) was studied by measuring the real part (ε_r') and the imaginary part (ε_r'') of the relative permittivity as a function of frequency, and the results are shown in Figure 6. The ε_r' gradually decreased with increasing the frequency (Figure 6A),

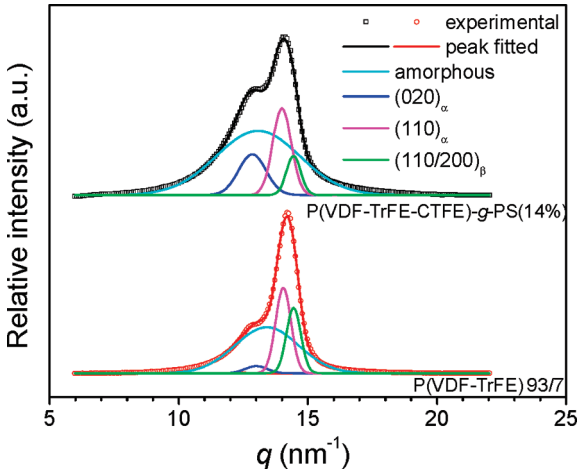

Figure 5. 1D WAXD profiles for P(VDF-TrFE) 93/7 and P(VDF-TrFE-CTFE)-*g*-PS(14%). Peak-fitting is performed to determine α and *β* crystal contents.

which is typical for ferroelectric polymers. Intriguingly, grafting only 14 wt % PS decreased the ε_r' by nearly 30%, i.e., from 12.6 for P(VDF-TrFE) 93/7 to 9.0 for P(VDF-TrFE-CTFE)-*g*-PS(14%) at 1.0 kHz (Figure 6A). The relaxation peaks at 1 MHz in Figure 6B originated from molecular motions of defects in PVDF crystals.[26,45,46] These defects included chain folds at the amorphous−crystalline interface, conformational disorder at interfaces between α/*β* or α/*γ* crystalline phases, and grain boundaries among small crystallites. Again, grafting only 14 wt % PS decreased the ε_r'' by nearly 40%, i.e., from 2.1 for P(VDF-TrFE) 93/7 to 1.2 for P(VDF-TrFE-CTFE)-*g*-PS(14%) at 1 MHz. We speculate that after P(VDF-TrFE) crystallization PS side chains were excluded to the periphery of P(VDF-TrFE) crystals, forming a nanoscale confining layer at the amorphous−crystalline interface (see the schematic in Figure 11B). It is this confining layer that reduced the molecular motions and thus amorphous dipole orientation at the amorphous−crystalline interface.

The ferroelectric and antiferroelectric-like behaviors in P(VDF-TrFE) 93/7, P(VDF-HFP) 96/4, and P(VDF-TrFE-CTFE)-*g*-PS(14%) were studied by *D*−*E* loop measurements. Figure 7A shows the hysteresis loops for P(VDF-TrFE) 93/7. Below 200 MV/m, propeller-shaped double hysteresis loops were observed, indicative of a two-step dipole reorientation process with the first step returning to the so-called antiferroelectric-like state.[26,27,38,39] Note that this antiferroelectric-like state is different from conventional antiferroelectric phases in ceramics and liquid crystals because it does not represent a new crystalline phase for PVDF and its copolymers (note that antiferroelectric or paraelectric *β*-phase does not exist). Instead, it represents a state that part of aligned dipoles and/or aligned ferroelectric domains revert to the opposite direction and the net dipole moment appears to be nearly zero. On the basis of a previous report,[27] this should be typical for PVDF and its

Table 1. Crystallinity, Melting Points, α and *β* Crystal Contents, and Estimated Average Crystallite Sizes for α and *β* Crystals in the Hot-Pressed and Stretched P(VDF-TrFE) 93/7 and P(VDF-TrFE-CTFE)-*g*-PS(14%) Films

films	crystallinity (wt %)[a]	T_m (°C)[a]	α (wt %)[b]	*β* (wt %)[b]	$D_{(110)\alpha}$ (nm)[b]	$D_{(110/200)\beta}$ (nm)[b]
P(VDF-TrFE) 93/7	44.1	156/168	27.7	17.6	17	17
P(VDF-HFP) 96/4	43.3	146	35.2	2.7	10 (∥); 23(⊥)[c]	11 (∥)
P(VDF-TrFE- CTFE)-*g*-PS(14%)	31.8 (39.6)	158	31.5	6.5	14	19

[a] Determined by differential scanning calorimetry (DSC). The crystallinity is the overall crystallinity, including PS in the amorphous part. The crystallinity inside the parentheses refers to the true crystallinity after normalized to the PVDF weight percentage. The heat of fusion of the perfect PVDF crystal is 102.5 J/g, assuming the same for all crystalline forms.[44] [b] Determined by 1D wide-angle X-ray diffraction (WAXD) in Figure 5. The crystallite size was estimated by the Scherrer equation. [c] The solution-cast and stretched P(VDF-HFP) 96/4 film has two types of crystal orientation with respect to the uniaxial drawing direction. The parallel crystals have a $D_{(110)\alpha}$ of 10 nm, and the perpendicular crystals have a $D_{(110)\alpha}$ of 23 nm.

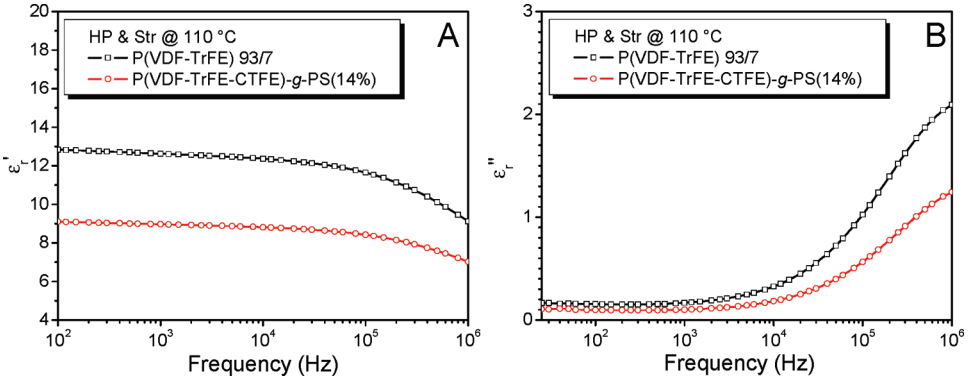

Figure 6. (A) Real part (ε_r') and (B) imaginary part (ε_r'') of the relative permittivity for P(VDF-TrFE) 93/7 and P(VDF-TrFE-CTFE)-*g*-PS(14%).

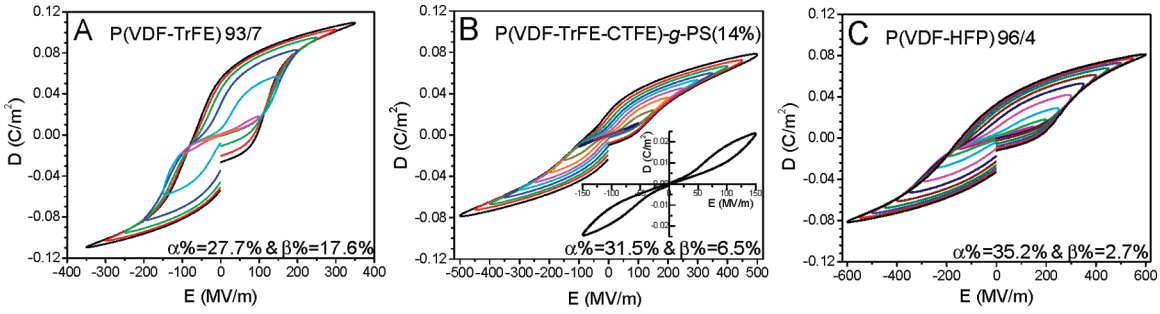

Figure 7. Bipolar $D-E$ hysteresis loops for (A) P(VDF-TrFE) 93/7, (B) P(VDF-TrFE-CTFE)-*g*-PS(14%) graft copolymer, and (C) solution-cast and stretched P(VDF-HFP) 96/4 (adapted from ref 27). The poling field has an increment of 50 MV/m at each step until the film breaks down electrically.

copolymers with a reduced compensation polarization at relatively low poling fields. At high poling fields (>200 MV/m), this antiferroelectric-like behavior disappeared because the compensation polarization became strong enough and ferroelectric behavior dominated in samples (see the normal ferroelectric hysteresis loops at >200 MV/m in Figure 7A). For P(VDF-TrFE-CTFE)-*g*-PS(14%) in Figure 7B, however, propeller-shaped double hysteresis loops persisted up to at least 400 MV/m. The inset of Figure 7B shows a typical antiferroelectric-like $D-E$ loop with very small remanent polarization at the zero field (compare with Scheme 1C). With a gradual increase of the poling field, the effect of double hysteresis loop became gradually reduced. One might argue that this difference between P(VDF-TrFE) 93/7 and P(VDF-TrFE-CTFE)-*g*-PS(14%) could be attributed to the low β crystal content in the graft copolymer. To address this problem, $D-E$ hysteresis loops for the solution-cast and stretched P(VDF-HFP) 96/4 film, which had similar α and β crystal contents (α% = 35.2 wt % and β% = 2.7 wt %) as the graft copolymer (α% = 31.5 wt % and β% = 6.5 wt %), are shown in Figure 7C. Although the antiferroelectric-like behavior was seen below 300 MV/m, double hysteresis loops completely disappeared above 350 MV/m. This result indicated that the high field antiferroelectric-like behavior in P(VDF-TrFE-CTFE)-*g*-PS(14%) could not be simply explained by a low β crystal content in the sample.

Figure 8 further quantifies our observation in Figure 7 by plotting the maximum and remanent electric displacement (D_{max} and D_{rem}) as a function of electric field for P(VDF-TrFE) 93/7, P(VDF-TrFE-CTFE)-*g*-PS(14%), and P(VDF-HFP) 96/4. Between 100 and 200 MV/m, there was a steplike increase in D_{max} for P(VDF-TrFE) 93/7. This could be attributed to the crystalline dipole switching (or alignment) with increasing the electric field as well as an increase in the induced compensation polarization in the amorphous phase (see Figure 11A). As a result, the D_{rem} also increased in this electric field range because of an increased number of persistent and aligned dipoles even when the electric field decreased to zero. Below 200 MV/m, a relatively low D_{rem} and high D_{max} were consistent with the antiferroelectric-like behavior seen in Figure 7A. On the contrary, P(VDF-TrFE-CTFE)-*g*-PS(14%) exhibited slow and monotonic increases in both D_{max} and D_{rem} as a function of electric field. We speculate that the induced compensation polarization was reduced by the low polarizability PS-rich interfacial layer between the crystalline and amorphous P(VDF-TrFE). Again, the extremely low D_{rem} and relatively high D_{max} in P(VDF-TrFE-CTFE)-*g*-PS(14%) were a clear indication of the antiferroelectric-like behavior. For P(VDF-HFP) 96/4, both D_{max} and D_{rem} were low below 300 MV/m due to the antiferroelectric-like behavior seen

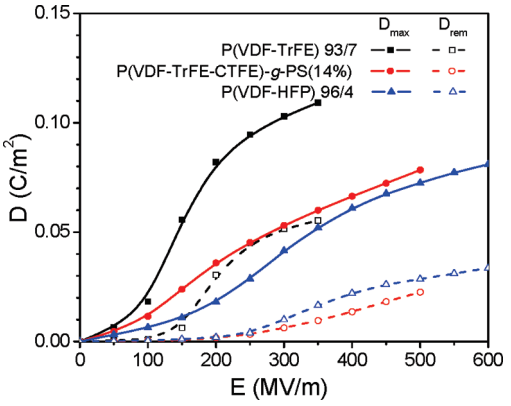

Figure 8. Maximum electric displacement (D_{max}) and remanent electric displacement (D_{rem}) as a function of electric field for P(VDF-TrFE) 93/7, P(VDF-TrFE-CTFE)-*g*-PS(14%) graft copolymer, and P(VDF-HFP) 96/4.

in Figure 7C. Above 350 MV/m, both D_{max} and D_{rem} exhibited apparent increases because of the disappearance of double hysteresis loops.

Further differences between P(VDF-TrFE-CTFE)-*g*-PS and P(VDF-HFP) 96/4 are demonstrated in the following experiments. First, P(VDF-HFP) 96/4 and P(VDF-TrFE-CTFE)-*g*-PS(14%) films were stepwise poled unipolarly up to 600 MV/m at a step of 50 MV/m (see Figure S4 in the Supporting Information). Then, both films were poled bipolarly at 250 MV/m for four continuous cycles, and the results are shown in Figure 9. For P(VDF-HFP) 96/4, the double hysteresis loop only appeared in the first cycle and disappeared in the rest cycles (see Figure 9A). However, the double hysteresis loops still persisted even at the fourth cycle for P(VDF-TrFE-CTFE)-*g*-PS(14%) (see Figure 9B). We speculate that this difference should originate from possible phase transformations in the solution-cast and stretched P(VDF-HFP) 96/4 film after stepwise unipolar polarization up to 600 MV/m, but not in the P(VDF-TrFE-CTFE)-*g*-PS(14%) film. This is evidenced by comparison of the FTIR spectra before and after stepwise poling for P(VDF-HFP) 96/4 and P(VDF-TrFE-CTFE)-*g*-PS(14%), respectively, in Figure 10A. For P(VDF-HFP) 96/4, the β crystal absorption bands at 1279, 1073, and 842 cm^{-1} slightly increased their intensity (Figure 10A), suggesting slightly more β crystals were induced by electric poling to 600 MV/m. For P(VDF-TrFE-CTFE)-*g*-PS(14%), however, the FTIR spectrum after poling to 600 MV/m nearly overlapped with the spectrum before poling

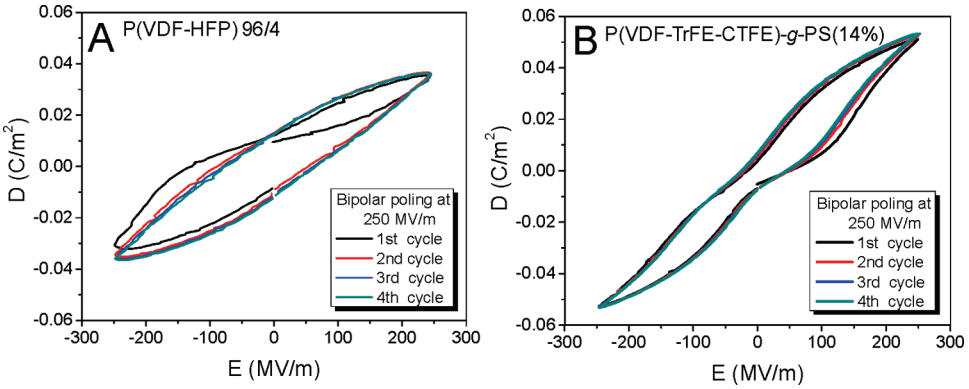

Figure 9. After stepwise unipolar poling up to 600 MV/m at a step of 50 MV/m, (A) P(VDF-HFP) 96/4 and (B) P(VDF-TrFE-CTFE)-*g*-PS(14%) were bipolarly polarized at 250 MV/m for four continuous cycles.

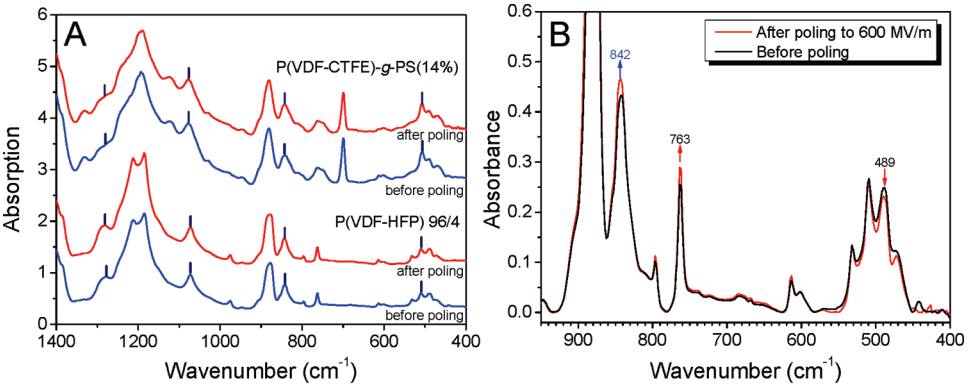

Figure 10. (A) FTIR spectra for P(VDF-HFP) 96/4 and P(VDF-TrFE-CTFE)-*g*-PS(14%) before and after stepwise unipolar poling up to 600 MV/m at a step of 50 MV/m. Vertical bars indicate absorption bands for the β crystals. (B) shows a magnified region (400−950 cm^{-1}) for P(VDF-HFP) 96/4 in (A). Baselines have been subtracted for both curves.

(Figure 10A), indicating that no $\alpha \rightarrow \beta$ phase transformation was observed due to the existence of relatively large PS side chains. All these experimental results clearly indicated that P(VDF-TrFE-CTFE)-*g*-PS(14%) was substantially different from P(VDF-HFP) 96/4. Note that paraelectric α PVDF crystals should not result in the large hysteresis loops at high electric fields for P(VDF-HFP) 96/4 (see Figure 7C). Instead, the polar δ crystals were responsible for large hysteresis loops after phase transformation from the α crystals above 150 MV/m. The $\alpha \rightarrow \delta$ phase transformation is evidenced in Figure 10B. It was seen that after poling to 600 MV/m the absorption band (B_u species for the α-phase) at 489 cm^{-1} decreased the intensity while the absorption band (A_u species for the α-phase) at 763 cm^{-1} increased the intensity. This result is consistent with the $\alpha \rightarrow \delta$ observations reported in the literature.[23]

Double hysteresis loops in P(VDF-TrFE) copolymers were first observed in 1981 by Yamada et al.[47] and later by Furukawa et al.[38−40] and Koizumi et al.[48] Yamada et al.[47] and Koizumi et al.[48] attributed the double hysteresis loops to the coexistence of the low temperature ferroelectric phase and high temperature paraelectric (disordered) phase, while Furukawa et al.[38−40] proposed a new antiferroelectric phase to explain the same phenomena. However, these explanations seemed to be restricted to P(VDF-TrFE) random copolymers. Recently, we proposed a universal mechanism to explain double hysteresis loops and generalized it to PVDF homopolymer and its random copolymers.[27] Following that work, the fundamental physics underlying this antiferroelectric-like behavior at high poling fields for P(VDF-TrFE-CTFE)-*g*-PS(14%) can be explained by the schematic models in Figure 11. Figure 11A shows the polarization mechanism for normal ferroelectric PVDF and its copolymers, which has been explained in detail in a previous report.[27] This model is adapted with modifications from the Lorentz local field model described in textbooks.[49,50] In brief, an external electric field, E, induces dipole orientations in both crystalline and amorphous phases. The alignment of dipoles inside the crystal produces a macroscopic polarization, P_{in}, which in turn is compensated by the polarization of the amorphous phase, P_{comp}. The P_{in} generates a local depolarization field, $E_{depol} = P_{in}/\varepsilon_0$, where ε_0 is the vacuum permittivity. The electric displacement on the electrodes generates a local polarization field, $E_{pol} = (Q + P_{comp})/\varepsilon_0 = (\varepsilon_0 E + P_{comp})/\varepsilon_0$, where Q is the vacuum polarization ($\varepsilon_0 E$). During dynamic switching processes, P_{in} may not equal P_{comp}, and the competition between local depolarization and polarization fields dictates the dipole switching behavior. When $E_{pol} > E_{depol}$, oriented dipoles will remain aligned, resulting in a high D_{rem}. When $E_{pol} < E_{depol}$, part of the aligned dipoles will revert to the opposite direction, resulting in an antiferroelectric-like state with a nearly zero polarization (i.e., a low D_{rem}). P_{in} is primarily a function of the dipole moment per repeat unit per chain and the number density of oriented dipoles in the crystal, and thus may not be easy to tune via changing molecular parameters for a given polymer (note that P_{in} changes with the poling field). P_{comp} is a function of the number density of

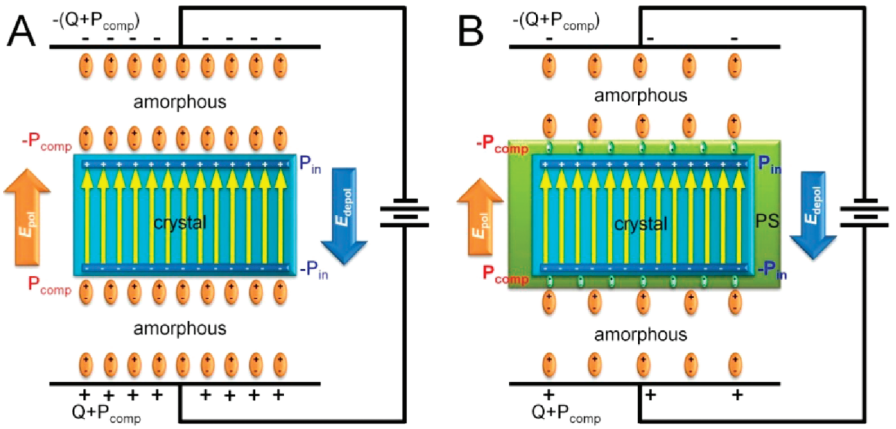

Figure 11. Schematic models of polarization mechanisms for (A) P(VDF-TrFE) and (B) P(VDF-TrFE-CTFE)-*g*-PS. Note that after PVDF crystallization the grafted PS side chains form a nanoscale interfacial layer (green color) around the ferroelectric crystal (blue color). Note that the (folded) PVDF chain axes are in the horizontal direction in the crystals (not drawn for clarity).

polarizable dipoles ($N_{0,am}$), the polarizability (α_{am}), and the local electric field ($E_{L,am}$) of the amorphous phase at the amorphous−crystalline interface; $P_{comp}=N_{0,am}\alpha_{am}E_{L,am}$. Therefore, P_{comp} can be easily adjusted by varying $N_{0,am}$ and α_{am}, and an effective way to induce the antiferroelectric-like state is to reduce P_{comp}, as we mentioned before.

As shown in Figure 11B, a low polarizability PS-rich interfacial layer is utilized to confine the P(VDF-TrFE) crystal after the crystallization-induced microphase separation. Although we performed transmission electron microscopy study on microtomed thin sections stained by RuO_4, no clear nanocrystalline lamellae were seen. It was possible that the PS grafts were too short (only three repeating units) and thus were miscible with surrounding amorphous P(VDF-TrFE) chains. This made RuO_4 staining difficult or not enough to provide good contrast. However, the crystalline lamellar morphology in the crystallized P(VDF-TrFE-CTFE)-*g*-PS(14%) was evidenced by the SAXS at 25 °C. In Figure 3, a weak second-order reflection was seen at $2q^* = 0.50\ nm^{-1}$ after crystallization. We also calculated the average PS grafting density in P(VDF-TrFE-CTFE)-*g*-PS(14%) to see if it was reasonable to assume the nanocrystalline structure in Figure 11B. Since the number-average molecular weight of P(VDF-TrFE-CTFE) is 93 400 g/mol, one chain contains 1400 total repeating units. If we assume a totally random distribution of 3.5 mol % CTFE along the main chain, every 28 VDF/TrFE repeating units will contain one CTFE. After grafting styrene from CTFE, there should be 28 VDF/TrFE repeating units per PS side chain. If we assume a TGTG′ conformation in the α or δ crystal forms (*c*-axis = 0.496 nm), the lamellar thickness should be 3.5 nm. If we assume a zigzag conformation in the β form (*c*-axis = 0.256 nm), the calculated lamellar thickness is 7.1 nm. These lamellar thicknesses should be reasonable for randomly grafted copolymers (e.g., linear low-density polyethylene[51]). If the grafting is nonstatistical, the lamellar thickness could be even higher. Therefore, it is reasonable to assume the nanocrystalline lamellar morphology for P(VDF-TrFE-CTFE)-*g*-PS(14%), as shown in Figure 11B. The polarizability of the amorphous PS-rich phase near the ferroelectric crystal becomes much smaller because of the low polarizability of PS. As a result, the P_{comp} in P(VDF-TrFE-CTFE)-*g*-PS(14%) greatly decreases (see Figure 11B), as compared with that in P(VDF-TrFE) (see Figure 11A). During reverse poling (or discharged), the E_{pol} will be lower than the E_{depol}, and finally the crystalline dipoles aligned at a high electric field will easily revert to the opposite direction, resulting in an antiferroelectric-like behavior at high poling fields with a low D_{rem} and a reduced ferroelectric loss. Note that P_{comp} is experimentally measurable from $D-E$ hysteresis loops, whereas P_{in} is very difficult to determine experimentally. Currently, we are performing computer simulation to better understand the competition between E_{depol} (or P_{in}) and E_{pol} (or $Q + P_{comp}$) under different electric fields. However, this topic is outside the scope of current work and will be introduced in future publications.

Using the above electrostatic models, we can unify the underlying mechanism for the antiferroelectric-like behaviors in P(VDF-FHP) 93/7, P(VDF-TrFE-CTFE)-*g*-PS(14%), and P(VDF-HFP) 96/4. For P(VDF-TrFE) 93/7, P_{comp} is low at low electric fields. For P(VDF-TrFE-CTFE)-*g*-PS(14%), P_{comp} is low after grafting nonpolar PS side chains up to 500 MV/m. For P(VDF-HFP) 96/4, P_{comp} is low at a low β crystal content up to 300 MV/m. Therefore, whenever P_{comp} is low, the antiferroelectric-like behaviors will be observed (see Figure 7).

Electric Energy Storage and Discharge. When an electric field is applied on a dielectric material with a high density of orientational permanent dipoles, the dipoles are oriented along the field, and a majority part of the electric energy is stored during this poling/orientation process. This part of stored electric energy can only be released when the oriented dipoles quickly switch back to an antiferroelectric-like or a random state at a zero electric field during the discharge process. During the reverse poling process, dipoles will be poled along the reverse direction and the electric energy storage starts in the reverse direction. Therefore, the dipole switching behavior is critical to the electric energy storage and discharge behaviors, and an antiferroelectric-like dipole switching behavior is desirable because of a low fraction of undischarged energy density.

The charged and discharged electric energy densities were directly integrated from the bipolar $D-E$ loops, and results are shown in parts A and B of Figure 12, respectively. Above 200 MV/m, there was a large decrease in the stored energy density for P(VDF-TrFE-CTFE)-*g*-PS(14%) when compared with P(VDF-TrFE) 93/7, and the percentage of decrease (~45%) was much larger than the weight fraction of PS (14 wt %). Therefore, it was reasonable to attribute this large decrease in the stored energy density to the significantly reduced compensation polarization, P_{comp} (see Figure 11B). Contrary to the stored energy density,

dx.doi.org/10.1021/ma102910v |*Macromolecules* 2011, 44, 2190–2199

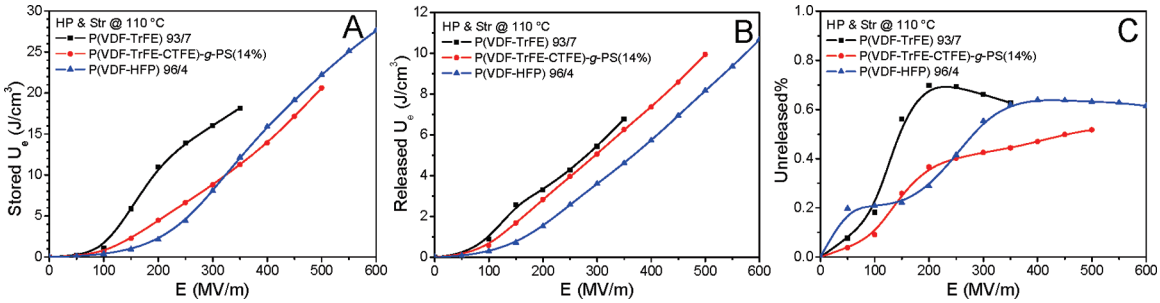

Figure 12. (A) Stored and (B) released electric energy densities and (C) unreleased% as a function of electric field for P(VDF-TrFE) 93/7 and P(VDF-TrFE-CTFE)-*g*-PS(14%) graft copolymer.

the discharge energy density for P(VDF-TrFE-CTFE)-*g*-PS-(14%) was just slightly lower than that for P(VDF-TrFE) 93/7, and the percentage of difference above 200 MV/m was only 13%. This again could be attributed to the low remanent polarization because of the antiferroelectric-like behavior for the graft copolymer. The unreleased part of energy density is defined as unreleased% = $100(1 - U_{e,\text{released}}/U_{e,\text{stored}})$, and results are shown in Figure 12C. The unreleased energy density was attributed to both ferroelectric and conduction losses during the bipolar switching process at high fields.[6,52] Note that the conduction loss became significant for polymers above 300−400 MV/m.[52] From Figure 12C, the ferroelectric/conduction loss was much lower in P(VDF-TrFE-CTFE)-*g*-PS(14%) than in P(VDF-TrFE) 93/7. The differences between P(VDF-TrFE-CTFE)-*g*-PS(14%) and P(VDF-HFP) 96/4 are also shown in Figure 12. Although the stored energy densities were similar, the released energy density for P(VDF-TrFE-CTFE)-*g*-PS(14%) was consistently higher than that for P(VDF-HFP) 96/4. Above 300 MV/m, the unreleased% for P(VDF-HFP) 96/4 was higher than that for P(VDF-TrFE-CTFE)-*g*-PS(14%) because of the gradual disappearance of the antiferroelectric-like behavior in P(VDF-HFP) 96/4 as the poling field exceeded 300 MV/m.

CONCLUSIONS

In summary, an antiferroelectric-like behavior with relatively narrow hysteresis loops and low remanent polarization was achieved in a P(VDF-TrFE-CTFE)-*g*-PS(14%) graft copolymer. The fast dipole reorientation to the antiferroelectric-like state upon discharging was explained by the reduced compensation polarization based on a confined ferroelectricity model, where the nanoscale P(VDF-TrFE) crystal was confined with a thin PS-rich interfacial layer (Figure 11B). It was because of the lower polarizability of the PS-rich interfacial layer than that of the amorphous P(VDF-TrFE) that the compensation polarization was significantly reduced. During reverse poling, the depolarization field could be higher than the polarization field. A significantly reduced ferroelectric loss and relatively high discharged energy density were observed in the P(VDF-TrFE-CTFE)-*g*-PS(14%) graft copolymer because of this antiferroelectric-like behavior even at high poling fields.

ASSOCIATED CONTENT

Supporting Information. Experimental setup for energy density measurements and unipolar $D-E$ hysteresis loops for P(VDF-HFP) 96/4 and P(VDF-TrFE-CTFE)-*g*-PS(14%) films, respectively. This material is available free of charge via the Internet at http://pubs.acs.org.

AUTHOR INFORMATION

Corresponding Author

*E-mail lxz121@case.edu; Tel (216) 368-5861.

ACKNOWLEDGMENT

The authors are indebted to Professors Jerome Lando and Donald Schuele at Case Western Reserve University for helpful discussions. This work was supported by ONR (N00014-05-1-0338) and NSF (DMR-0907580).

REFERENCES

(1) Sarjeant, W. J.; Zirnheld, J.; MacDougall, F. W. *IEEE Trans. Plasm. Sci.* **1998**, *26*, 1368–1392.
(2) Sarjeant, W. J.; Clelland, I. W.; Price, R. A. *Proc. IEEE* **2001**, *89*, 846–855.
(3) Tan, Q.; Irwin, P.; Cao, Y. *IEEJ Transactions on Fundamentals and Materials* **2006**, *126*, 1153–1159.
(4) Ducharme, S. *ACS Nano* **2009**, *3*, 2447–2450.
(5) Chu, B.; Zhou, X.; Ren, K.; Neese, B.; Lin, M.; Wang, Q.; Bauer, F.; Zhang, Q. M. *Science* **2006**, *313*, 1887–1887.
(6) Zhou, X.; Chu, B.; Neese, B.; Lin, M.; Zhang, Q. M. *IEEE Trans. Dielectr. Electr. Insul.* **2007**, *14*, 1133–1138.
(7) Kim, P.; Doss, N. M.; Tillotson, J. P.; Hotchkiss, P. J.; Pan, M. J.; Marder, S. R.; Li, J.; Calame, J. P.; Perry, J. W. *ACS Nano* **2009**, *3*, 2581–2592.
(8) Kim, P.; Jones, S. C.; Hotchkiss, P. J.; Haddock, J. N.; Kippelen, B.; Marder, S. R.; Perry, J. W. *Adv. Mater.* **2007**, *19*, 1001–1005.
(9) Lu, Y.; Claude, J.; Neese, B.; Zhang, Q.; Wang, Q. *J. Am. Chem. Soc.* **2006**, *128*, 8120–8121.
(10) Lu, Y.; Claude, J.; Zhang, Q.; Wang, Q. *Macromolecules* **2006**, *39*, 6962–6968.
(11) Jow, T. R.; Cygan, P. J. *J. Appl. Phys.* **1993**, *73*, 5147–5151.
(12) Zhou, X.; Zhao, X.; Suo, Z.; Zou, C.; Runt, J.; Liu, S.; Zhang, S.; Zhang, Q. M. *Appl. Phys. Lett.* **2009**, *94*, 162901.
(13) Claude, J.; Lu, Y.; Wang, Q. *Appl. Phys. Lett.* **2007**, *91*, 212904.
(14) Claude, J.; Lu, Y.; Li, K.; Wang, Q. *Chem. Mater.* **2008**, *20*, 2078–2080.
(15) Li, J.; Claude, J.; Norena-Franco, L. E.; Seok, S. I.; Wang, Q. *Chem. Mater.* **2008**, *20*, 6304–6306.
(16) Li, J.; Seok, S. I.; Chu, B.; Dogan, F.; Zhang, Q.; Wang, Q. *Adv. Mater.* **2009**, *21*, 217–221.
(17) Guo, N.; DiBenedetto, S. A.; Kwon, D. K.; Wang, L.; Russell, M. T.; Lanagan, M. T.; Facchetti, A.; Marks, T. J. *J. Am. Chem. Soc.* **2007**, *129*, 766–767.
(18) Guo, N.; DiBenedetto, S. A.; Tewari, P.; Lanagan, M. T.; Ratner, M. A.; Marks, T. J. *Chem. Mater.* **2010**, *22*, 1567–1578.
(19) An, L.; Boggs, S. A.; Callame, J. P. *IEEE Electr. Insul. Mag.* **2008**, *24*, 5–10.
(20) Calame, J. P. *J. Appl. Phys.* **2006**, *99*, 084101.
(21) Brus, L. *Acc. Chem. Res.* **2008**, *41*, 1742–1749.

(22) Lovinger, A. J. *Science* **1983**, *220*, 1115–1121.
(23) Tashiro, K. Crystal Structure and Phase Transition of PVDF and Related Copolymers. In *Ferroelectric Polymers: Chemistry, Physics, and Applications*, 1st ed.; Nalwa, H. S., Ed.; Dekker: New York, 1995; pp 63−182.
(24) Mizutani, T.; Yamada, T.; Ieda, M. *J. Phys. D: Appl. Phys.* **1981**, *14*, 1139–1147.
(25) Starkweather, J., H. W.; Avakian, P.; Matheson, R. R.; Fontanella, J. J.; Wintersgill, M. C. *Macromolecules* **1992**, *25*, 6871–6875.
(26) Guan, F.; Pan, J.; Wang, J.; Wang, Q.; Zhu, L. *Macromolecules* **2010**, *43*, 384–392.
(27) Guan, F.; Wang, J.; Pan, J.; Wang, Q.; Zhu, L. *Macromolecules* **2010**, *43*, 8209–8217.
(28) Guan, F.; Yuan, Z.; Shu, E. W.; Zhu, L. *Appl. Phys. Lett.* **2009**, *94*, 052907.
(29) Chu, B.; Zhou, X.; Neese, B.; Zhang, Q. M.; Bauer, F. *IEEE Trans. Dielectr. Electr. Insul.* **2006**, *13*, 1162–1169.
(30) Ranjan, V.; Yu, L.; Nardelli, M. B.; Bernholc, J. *Phys. Rev. Lett.* **2007**, *99*, 047801.
(31) Kittel, C. *Phys. Rev.* **1951**, *82*, 729–732.
(32) Park, S. E.; Pan, M. J.; Markowski, K.; Yoshikawa, S.; Cross, L. E. *J. Appl. Phys.* **1997**, *82*, 1798–1803.
(33) Park, Y. *J. Phys. Chem. Solids* **1998**, *59*, 1423–1428.
(34) Xu, B.; Ye, Y.; Cross, L. E. *J. Appl. Phys.* **2000**, *87*, 2507–2515.
(35) Xu, B.; Cross, L. E.; Bernstein, J. J. *Thin Solid Films* **2000**, *377*, 712–718.
(36) Urruchi, V.; Perez, I.; Pena, J. M. S.; Torres, J. C.; Castillo, P. L.; Quintana, X.; Oton, J. M. *Mol. Cryst. Liq. Cryst.* **2006**, *450*, 217–228.
(37) Furukawa, T.; Date, M.; Fukada, E. *J. Appl. Phys.* **1980**, 1135–1141.
(38) Furukawa, T.; Lovinger, A. J.; Davis, G. T.; Broadhurst, M. G. *Macromolecules* **1983**, *16*, 1885–1890.
(39) Takahashi, Y.; Kodama, H.; Nakamura, M.; Furukawa, T.; Date, M. *Polym. J.* **1999**, *31*, 263–267.
(40) Furukawa, T.; Takahashi, Y. *Ferroelectrics* **2001**, *264*, 1739–1748.
(41) Zhang, M.; Russell, T. P. *Macromolecules* **2006**, *39*, 3531–3539.
(42) Sakamoto, N.; Hashimoto, T. *Macromolecules* **1995**, *28*, 6825–6834.
(43) Sakamoto, N.; Hashimoto, T. *Macromolecules* **1998**, *31*, 3815–3823.
(44) Mead, W. T.; Zachariades, A. E.; Shimada, T.; Porter, R. S. *Macromolecules* **1979**, *12*, 473–478.
(45) Furukawa, T.; Wang, T. Measurements and Properties of Ferroelectric Polymers. In *The Applications of Ferroelectric Polymers*; Wang, T., Herbert, J. M., Glass, A. M., Eds.; Chapman and Hall: New York, 1988; Vol. 5, pp 66−117.
(46) Hahn, B.; Wendorff, J.; Yoon, D. Y. *Macromolecules* **1985**, *18*, 718–721.
(47) Yamada, T.; Ueda, T.; Kitayama, T. *J. Appl. Phys.* **1981**, *52*, 948–952.
(48) Koizumi, N.; Murata, Y.; Tsunashima, H. *IEEE Trans. Electr. Insul.* **1986**, *21*, 543–548.
(49) Blythe, A. R. *Electrical Properties of Polymers*; Cambridge University Press: Cambridge, 1979; pp 15−37.
(50) Ku, C. C.; Liepins, R. *Electrical Properties of Polymers: Chemical Principles*; Hanser Publishers: New York, 1987; pp 28−30.
(51) Hosoda, S.; Nozue, Y.; Kawashima, Y.; Utsumi, S.; Nagamatsu, T.; Wagener, K.; Berda, E.; Rajas, G.; Baughman, T.; Leonard, J. *Macromol. Symp.* **2009**, *282*, 50–64.
(52) Chen, Q.; Wang, Y.; Zhou, X.; Zhang, Q. M.; Zhang, S. *Appl. Phys. Lett.* **2008**, *92*, 142909.

■ NOTE ADDED AFTER ASAP PUBLICATION

This article posted ASAP on March 2, 2011. Throughout the paper, "remnant" was changed to "remanent". The correct version posted on March 9, 2011.